

High Capacity Prussian Blue Analogue@Reduced Graphene Oxide/Li₄Ti₅O₁₂ Composite as an Anode Material for Lithium-Ion Batteries with a Broad Voltage Window

Daming Sun^{1,2}, Huan Zhang^{1,2}, Hao Wang¹, Bangwei Deng^{1,2}, Yan Ding^{1,2}, Xuan Li^{1,2}, Jianbin Li^{1,2}, Wujie Ge^{3,*}, Meizhen Qu^{1,2,*}

¹ Chengdu Institute of Organic Chemistry, Chinese Academy of Sciences (CAS), No. 9, 4th section of South Renmin Road, Chengdu 610041, P. R. China

² University of Chinese Academy of Sciences, No. 19 (A) Yuquan Road, Beijing 100049, P. R. China

³ School of Chemical Engineering, Guizhou Institute of Technology, Guiyang, 550003, P. R. China

*E-mail: gewj0359@163.com, mzhqu18@cioc.ac.cn

Received: 18 February 2019 / Accepted: 8 April 2019 / Published: 10 May 2019

A narrow electrochemical window, poor electronic conductivity and lithium ions transfer capability slow down the mass application of Li₄Ti₅O₁₂ (LTO) as power batteries in passenger cars with a long range. An effective way to improve the capacity and energy density of LTO is to include it in a composite materials to provide a good ionic and electronic conductive network followed by excess discharge to about 0 V vs. Li⁺/Li. Mn-Fe based Prussian blue analogue (Mn-PBA) nanoparticles with special open framework structure anchor on the reduced graphene oxide (rGO) conferred a high electronic and ionic conductivity and similar charge/discharge voltage plateaus with LTO. As a result, the Mn-PBA@rGO/LTO composite takes full advantages of high capacity Mn-PBA and the high electronic conductivity rGO sheets. It delivered a high reversible capacity (301.7 mAh g⁻¹ at 0.2 C) and superior rate performance (208.5 mAh g⁻¹ at 30 C) in a broad electrochemical voltage range between 0.01 and 3 V in half cells. Furthermore, a capacity of 232.6 mAh g⁻¹ at 1 C of Mn-PBA@rGO/LTO–10% was measured and good cycling performance was obtained in pouch cells with LiNi_{0.6}Co_{0.2}Mn_{0.2}O₂ (NCM622) as a cathode and Mn-PBA@rGO/LTO–10% as anode, indicating that the Mn-PBA@rGO/LTO–10% composite is a promising anode material for lithium-ion batteries (LIBs).

Keywords: Prussian blue analogue@reduced graphene oxide; Li₄Ti₅O₁₂; composite anode; broad voltage window; Lithium-ion batteries.

1. INTRODUCTION

The zero-strain spinel Li₄Ti₅O₁₂ (LTO) has been used as a commercial anode material for Lithium-ion batteries (LIBs) because of its good structural stability [1, 2], excellent high and low temperature performance, long cycling life and safety [3]. However, the low energy density due to the

relatively high lithium insertion potential and low theoretical capacity of 175 mAh g⁻¹ during the constant discharge/charge in the 1–3 V vs. Li⁺/Li voltage range cannot meet the increasingly critical requirements for commercial LIBs [4, 5].

Numerous strategies have been proposed to improve the capacity of LTO including surface modification [6, 7], morphological changes [8, 9], heterogeneous element doping [10, 11], insertion in composite materials [12, 13], and excess discharge near 0 V [14, 15]. Among all these, the fabrication of composites with other materials that have a high electronic and ionic conductivity could effectively improve the performance and reversible capacity of LTO anode. For example, N-doped LTO decorated on TiC/C nanowires with a large specific area and high mechanical stability showed an outstanding rate 143 mAh g⁻¹ at 10 C [16]. A hybrid of three-dimensional hierarchical LTO-TiO₂/MoO₂ nanoclusters embedded into high conductivity carbon nanosheets achieved a high reversible specific capacity of 413 mAh g⁻¹ at 1000 mA g⁻¹ after 500 cycles [17]. Normally when LTO is placed at 1 V, only 60% Ti⁴⁺ is reduced to Ti³⁺, giving a capacity of 175 mAh g⁻¹ [18]. The reversible capacity of LTO can be greatly improved if Li₇Ti₅O₁₂ is further oxidized from 1.55 V to 0 V [19]. However, Han found that LTO exhibited a rapidly fading specific capacity which was caused by reduced lithium-ion diffusion and charge transfer from the increased resistance and polarization when cycled down to 0 V at high rates (>10 C) [14]. Therefore, making LTO composites with other materials to provide good ionic and electronic conductive networking and extending the lithiation voltage to 0 V vs. Li⁺/Li is a promising way to increase the specific capacity and energy density of LTO anode [3].

In this work, a Mn-Fe based Prussian blue analogue@reduced graphene oxide (Mn-PBA@rGO) was physically mixed with LTO to constitute an anode material for LIBs. The three-dimensional (3-D) open framework structure of Mn-PBA with its high ionic conductivity combined to the high electrical conductivity of rGO can accelerate the diffusion of electrons and lithium ions in the Mn-PBA@rGO/LTO electrode. The improved reversible capacity, especially at a high charge/discharge rate, illustrated that the Mn-PBA@rGO/LTO composite is an excellent anode material for high power output LIBs.

2. EXPERIMENTAL

2.1 Material preparation

The Mn-PBA@rGO composite was synthesized according to our previously published procedure [20]. The Mn-PBA@rGO/LTO–10% anode was obtained by mixing Mn-PBA@rGO and LTO (XNT160, Sichuan XingNeng New Materials Co., Ltd., China) with a mass ratio of 10%. All reagents were used as purchased from the manufacturer without further treatment.

2.2 Material characterization

X-ray diffraction (XRD) (D8 ADVANCE A25X, Bruker, Germany) with a Cu K α radiation was used to characterize the crystal structure of LTO and Mn-PBA@rGO/LTO–10% at the 2 θ scale between

5 and 80°. The morphology of the samples was determined by scanning electron microscopy (SEM) (JSM-7500F, JEOL, Japan). The valences of each element were determined by X-ray photoelectron spectroscopy (XPS) (Escalab 250Xi, Thermo Fisher Scientific, UK).

2.3 Electrochemical measurements

The working electrode was composed of active material (80%), LA133 binder (10%, Chengdu Indigo Power Sources Co., Ltd., China), and Super P (10%, Imerys Graphite & Carbon, Switzerland). All constituents were coated on 15 μm thick copper foil. Subsequently, the electrode was dried at 105 °C in vacuum for 12 h. The mass loading of the active material was about 0.88 mg cm^{-2} . 2032 coin cells were fabricated with such working electrodes, a polypropylene membrane separator (Celgard 2400, LLC, USA), and Li metal (China Energy Lithium Co., Ltd., China) in an argon-filled glove box ($\text{O}_2 < 0.1$ ppm, $\text{H}_2\text{O} < 0.1$ ppm, Chengdu Dellix Industry Co., Ltd., China). 2 wt% vinylene carbonate (VC) and 1 M LiPF_6 in diethyl carbonate (DEC)/ethylene carbonate (EC)/dimethyl carbonate (DMC) (1:1:1, v/v, Shenzhen Capchem Technology Co., Ltd., China) was used as the electrolyte. The discharge-charge tests were conducted within a voltage range of 0.01–3.0 V vs. Li^+/Li on a Neware battery measurement tester (CT-4008, Shenzhen Neware Technology Co., Ltd., China) at room temperature. All the cells were activated at 0.2 C for 2 cycles before testing for rate performance and cycling durability. All reversible specific capacities were calculated using LTO or Mn-PBA@rGO/LTO in the working electrode. Cyclic voltammetry (CV) was performed at a scan rate of 0.1 mV s^{-1} in the voltage range of 0.01 to 3.0 V on an Autolab M204 electrochemical workstation (Metrohm, Switzerland). The electrochemical impedance spectra (EIS) were recorded in the frequency range of 100 kHz to 0.01 Hz on the Autolab M204 electrochemical workstation. The pouch batteries were assembled with $\text{LiNi}_{0.6}\text{Co}_{0.2}\text{Mn}_{0.2}\text{O}_2$ (NCM622) as cathode and either LTO or Mn-PBA@rGO/LTO–10% as the anode. The positive electrode consisted of NCM622, Polyvinylidene fluoride (PVDF5130, Solef, USA), and Super P with a mass ratio of 92:2:6. The slurry was coated on aluminum foil and the typical mass loading of NCM622 was about 10.24 mg cm^{-2} , which was in high excess compared to the anode. Therefore, the specific capacity was calculated based on the mass of active component in the anode material. The cells were initially charged to 3.75 V at a constant charge (CC) of 0.1 C followed by charging at CC/constant voltage (CV) at a rate of 0.2 C at 4.3 V until the current gradually decreased to the cut-off current of 0.05 C. Subsequently, the cells were discharged to 1.5 V under CC of 0.2 C. For the next cycle, the CC/CV charging and CC discharging protocol was employed with voltages between of 1.5 and 4.3 V at a current rate of 1 C.

3. RESULTS AND DISCUSSION

The typical powder X-ray diffraction (XRD) patterns obtained are shown in Fig. 1a. The diffraction peaks at $2\theta = 18.33^\circ$, 30.18° , 35.57° , 37.21° , 43.24° , 47.37° , 57.21° , 62.83° , 66.07° , and 74.34° both in LTO and Mn-PBA@rGO/LTO-10% composite can be assigned to the (111), (220), (311), (222), (400), (331), (333), (440), (531), and (533) spinel LTO phase with a Fd-3m space group (PDF 49-

0207) [21-23]. This indicates that the LTO in both samples has a high crystallinity [9]. A typical diffraction peak at $2\theta=22.09^\circ$ in the Mn-PBA@rGO/LTO composite shows a cubic structure with a Fm-3m space group.

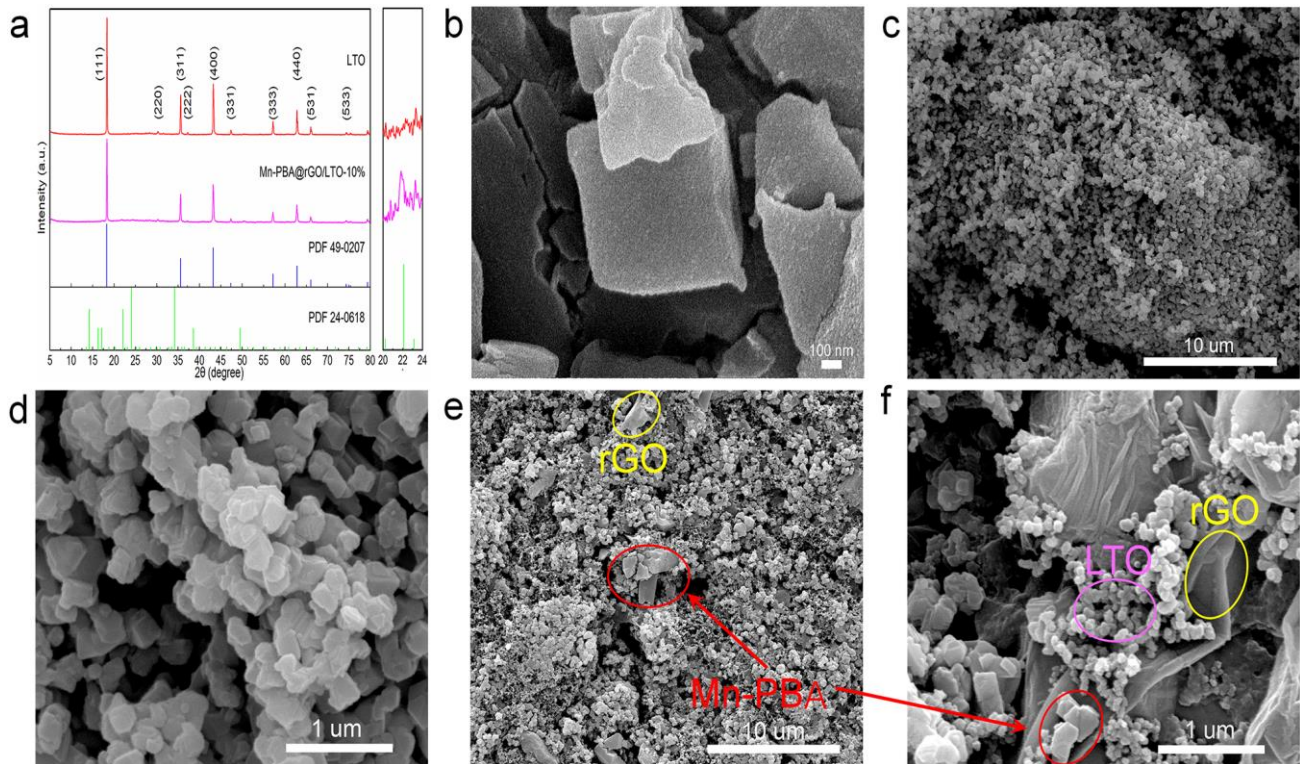


Figure 1. a) XRD patterns of LTO and Mn-PBA@rGO/LTO–10%; SEM images of b) Mn-PBA, c, d) LTO and e, f) Mn-PBA@rGO/LTO–10%.

The powder diffraction file (PDF 24–0618) of Mn-PBA in the composite material [24-26] is shown in Fig. 1a. The morphology and size of the samples prepared were determined by scanning electron microscopy (SEM). As shown in Fig. b, Mn-PBA is made up of abundant irregular cubic Mn-PBA nanoparticles. From Figs. 1 c and 1d, the irregular pristine LTO particles had a mean diameter of 200 nm and obvious self-aggregation. Figs. 1e and 1f showed a change in morphology after the inclusion in the Mn-PBA@rGO composite. More specifically, the LTO particles in the composite were partially anchored on the surface of rGO sheets and Mn-PBA nanoparticles.

The surface chemical valence and electrons state of elements in Mn-PBA@rGO/LTO–10% composite were determined by XPS. The survey spectrum in Fig. 2a indicated that the main peaks located at 285.0, 530.4, 399.1, 458.4, 641.5, and 708.1 eV could be ascribed to C1s, O1s, N1s, Ti2p, Mn2p, and Fe2p, respectively. There were no other impurities.

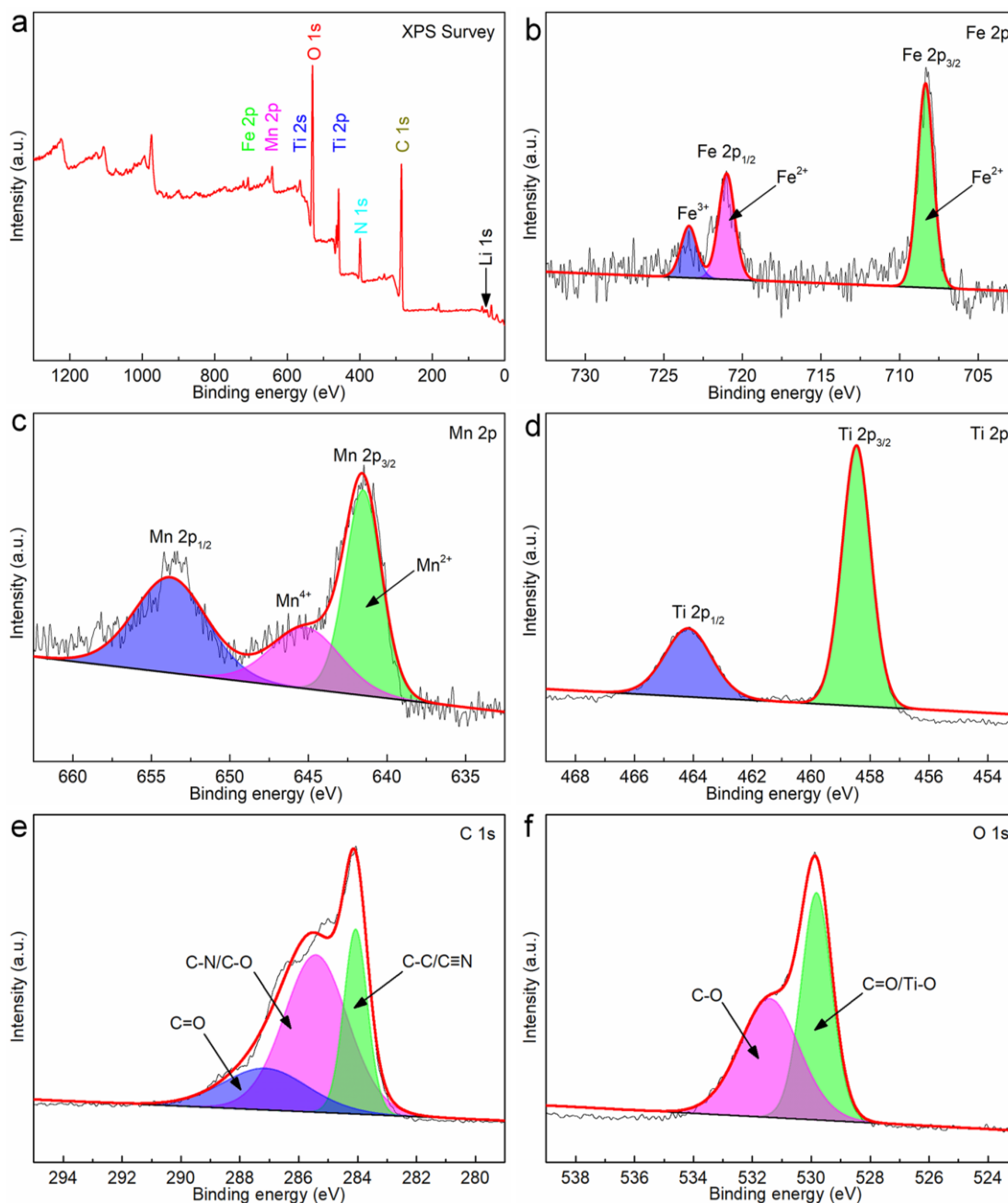


Figure 2. a) XPS survey spectrum of Mn-PBA@rGO/LTO-10% and sub-spectra of b) Fe 2p; c) Mn 2p; d) Ti 2p; e) C 1s; f) O 1s.

The high-resolution Fe2p spectrum in Fig. 2b can be divided into three peaks. The peaks at 708.1 and 721.0 eV belong to Fe $2p_{3/2}$ and Fe $2p_{1/2}$ in Fe $^{2+}$, whereas the peak at 723.4 eV corresponds to Fe $2p_{1/2}$ in Fe $^{3+}$, indicating the coexistence of Fe $^{2+}$ and Fe $^{3+}$ in the composite. The sub-spectrum of Mn2p in Fig. 2c can be fitted with three peaks located at 641.5, and 645.1 eV for Mn $2p_{3/2}$, and 653.7 eV for Mn $2p_{1/2}$, respectively. Fig. 2d shows the Ti2p spectrum, with one peak at 458.4 eV for Ti $2p_{3/2}$ and one peak at 464.1 eV for Ti $2p_{1/2}$ with an energy difference of 5.7 eV, indicating the presence of Ti $^{4+}$ in the spinel LTO particles [27-29]. Furthermore, the C1s spectrum in Fig. 2e is composed of three peaks at 284.0, 285.4, and 287.1 eV that can be assigned to C-C/C \equiv N, C-N/C-O and C=O groups, respectively. In Fig.

2f, the two cumulative peaks of O1s at 529.8 and 531.4 eV can be associated with C=O/Ti–O and C–O band, respectively.

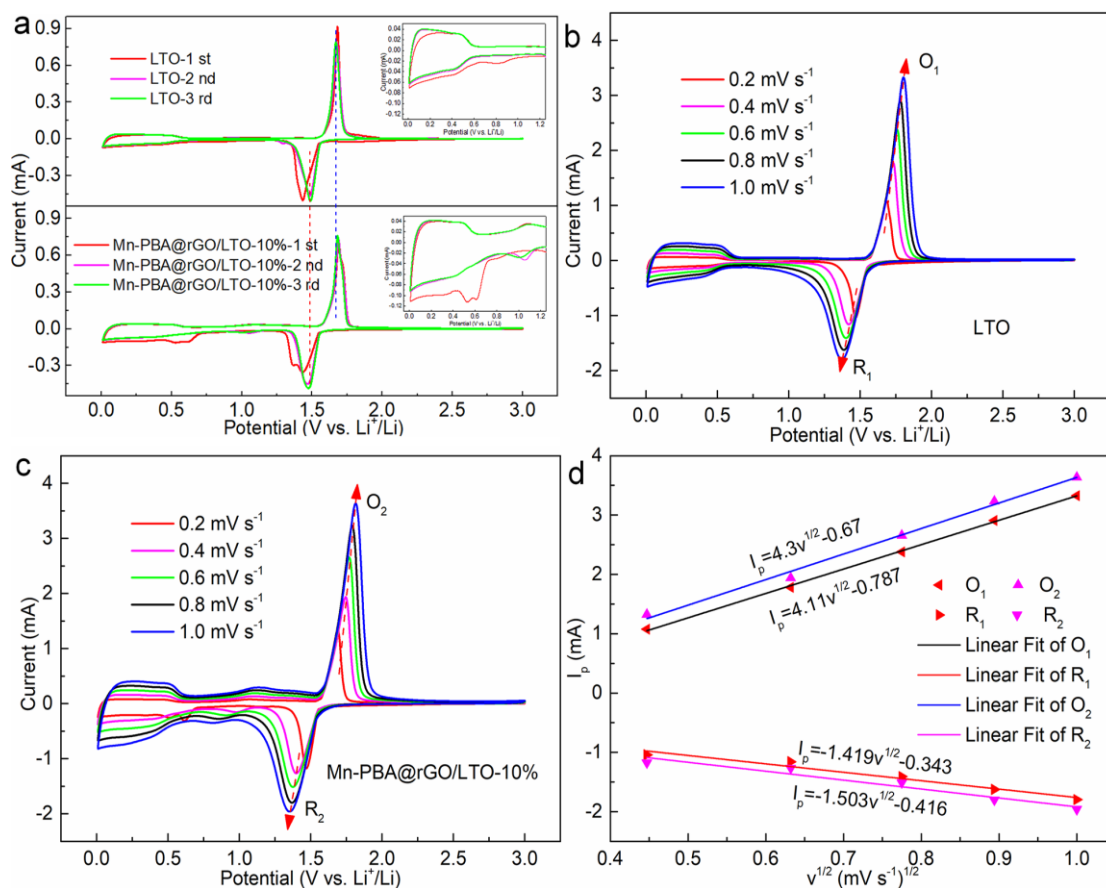


Figure 3. a) Cyclic voltammograms of LTO and Mn-PBA@rGO/LTO–10% showing the initial 3 cycles at a scan rate of 0.1 mV s⁻¹. The insets are zoom in selected areas; Voltammograms for b) LTO and c) Mn-PBA@rGO/LTO–10% at different scan rates from 0.2 to 1.0 mV s⁻¹ for voltages within 0.01 and 3 V vs. Li⁺/Li; d) Relationship between the peak current (I_p) and square root of scan rate (v^{1/2}) illustrative the diffusive nature of the peaks observed.

The electrochemical behaviors of LTO and Mn-PBA@rGO/LTO–10% were first measured by cyclic voltammetry (CV) at a scan rate of 0.1 mV s⁻¹ within a broad potential range of 0.01 to 3 V vs. Li⁺/Li, as shown in Fig. 3a. The well-defined peaks at 1.49 and 1.67 V can be attributed to the Ti⁴⁺/Ti³⁺ redox couple reaction [30], demonstrating a reversible phase transition from the spinel Li₄Ti₅O₁₂ to rock salt phase Li₇Ti₅O₁₂. During the first cathodic process, an additional peak at 1.36 V could be assigned to the reduction of high-valence Mn ions in the Mn-PBA@rGO/LTO–10% composite. In the following cycles, it merged with the peak at 1.46V, which may indicate a different phase transition of Mn-PBA in the first cycle. From the enlarged sections of the voltammograms, the peak at 0.8 V in LTO can be ascribed to the formation of solid electrolyte interface (SEI) films caused by the decomposition of electrolyte [31]. The peaks at 0.8 V and 0.53 V for Mn-PBA@rGO/LTO–10% also contained multiple

reductions of Mn and Fe ions [20]. In the next cycles, both peaks moved to higher potentials, which is a typical characteristic for a transition metal anode in LIBs [32-34].

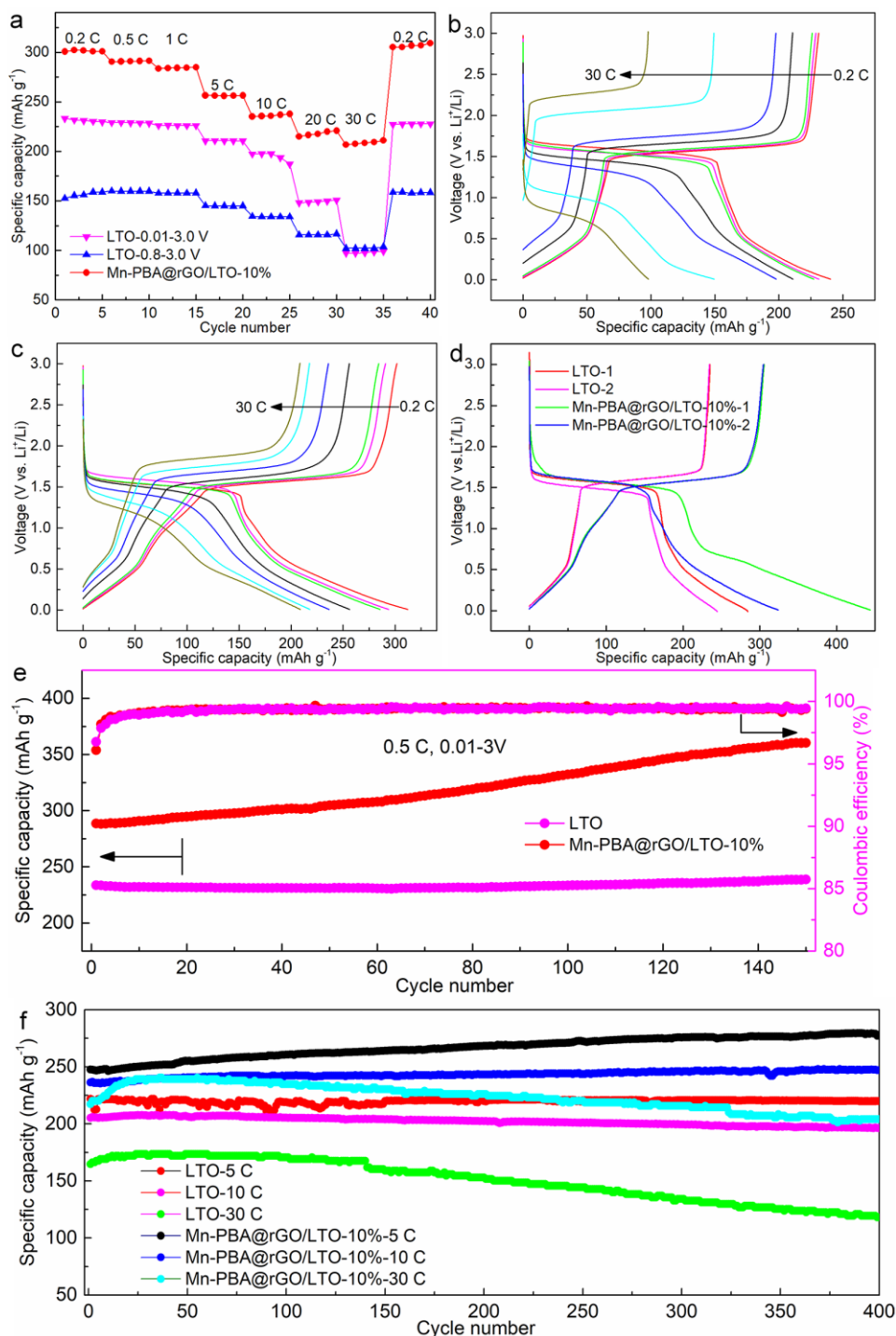


Figure 4. Electrochemical performance of LTO and Mn-PBA@rGO/LTO–10%. a) Rate capacities at various charge densities from 0.2 C to 30 C in the 0.01–3.0 V and 0.8–3.0 V voltage ranges; Corresponding discharge/charge curves for the third cycle at different current densities for b) LTO and c) Mn-PBA@rGO/LTO–10%; d) First and second galvanostatic discharge/charge curves at 0.2 C; e) Cycle performance with the coulombic efficiency at 0.5 C; f) Long-term cycling performance at 5, 10, and 30 C.

The peak at 0.61 V suggested an irreversible consumption of Li^+ on the surface of rGO layers [35]. The decreasing slope below 0.46 V was caused by the extra intercalation of lithium ions into $\text{Li}_7\text{Ti}_5\text{O}_{12}$ to form $\text{Li}_9\text{Ti}_5\text{O}_{12}$ [14]. The overlap between the oxidation peaks at 0.48, 1.09, 1.68, and 1.71 V after the first cycle showed that the electrochemical reaction in Mn-PBA@rGO/LTO-10% composite became relatively stable and had good reversibility.

The electrochemical kinetics of LTO and Mn-PBA@rGO/LTO-10% were investigated by recording CV curves at different scan rates from 0.2 to 1.0 mV s^{-1} , as shown in Figs. 3b and 3c. The reduction (R_1 and R_2) and oxidation (O_1 and O_2) peaks were shifted to lower and higher potentials, respectively, when the increasing of scan rates increased. In Fig. 3d, the clear linear relationship between the peak current (I_p) and square root of scan rate ($v^{1/2}$) indicated a diffusion-controlled electrochemical reaction process. Consequently, the diffusion coefficient of lithium ions (D_{Li^+}) can be calculated using the Randles-Sevcik equation [11, 36, 37]:

$$I_p = 2.69 \times 10^5 A n^{3/2} D_{\text{Li}^+}^{1/2} C_{\text{Li}^+} v^{1/2}$$

where A is the electrode area (1.13 cm^2), n is the number of transferred electrons (here $n=5$, corresponding to the conversion of $\text{Li}_4\text{Ti}_5\text{O}_{12}$ to $\text{Li}_9\text{Ti}_5\text{O}_{12}$), C_{Li^+} is the bulk concentration of lithium ions in the anode (approximately $8.74 \times 10^{-3} \text{ mol cm}^{-3}$) that can be calculated from the tap density ($\rho=0.95 \text{ g cm}^{-3}$) and the molecular weight ($M=109.747 \text{ g mol}^{-1}$). The calculated D_{Li^+} for Mn-PBA@rGO/LTO-10% ($1.60 \times 10^{-8} \text{ cm}^2 \text{ S}^{-1}$) was higher than the bare LTO electrode ($1.27 \times 10^{-8} \text{ cm}^2 \text{ S}^{-1}$). The improved lithium ions diffusion and speed of Mn-PBA@rGO/LTO-10% may depend on the coupling of Mn-PBA that with special 3-D open framework structure and large pore volume [9].

A comparison of the electrochemical performance of LTO and Mn-PBA@rGO/LTO-10% in the broad voltage range of 0.01 to 3.0 V is shown in Fig. 4. The rate performance of LTO and Mn-PBA@rGO/LTO-10% cycled from 0.2 C to 30 C in the broad voltage range from 0.01 to 3 V is indicated in Fig. 4a. Compared to bare LTO, Mn-PBA@rGO/LTO-10% exhibited higher reversible capacities of 301.7, 290.8, 284.2, 255.9, 235.8, 217.7, and 208.5 mAh g^{-1} than the LTO electrode (231.1, 228.8, 226.1, 210.8, 197.6, 149.2, and 97.9 mAh g^{-1}) at 0.2, 0.5, 1, 5, 10, 20, and 30 C, respectively. The specific capacity retention of the Mn-PBA@rGO/LTO-10% electrode (69.1%) was much higher than the bare LTO electrode (42.4%) at a high current density of 30 C, indicating the superior rate performance of Mn-PBA@rGO/LTO-10% electrode. Furthermore, when the current density was decreased back to 0.2 C, the specific capacity of Mn-PBA@rGO/LTO-10% (306.7 mAh g^{-1}) was slightly higher than the initial value (301.7 mAh g^{-1}), indicating a prominent reversibility of the composite electrode. In contrast, the reversible capacity (227.7 mAh g^{-1}) of the LTO electrode was slightly lower than the initial one (231.1 mAh g^{-1}). At high rate of 30 C, the specific capacity of LTO electrode (97.9 mAh g^{-1}) in the broad voltage range was lower than in the common voltage range from 0.8 to 3.0 V (103.6 mAh g^{-1}). This was attributed to the large polarization on the LTO electrode from the increased internal resistance during the excess discharge to near 0 V. This observation was highly consistent with a previous report [14]. Fig. 4b and 4c showed that the polarization of LTO was lower than for Mn-PBA@rGO/LTO-10% at low current rates of 0.2, 0.5, 1, 5, and 10 C. However, it increased when the current density was higher than 20 C. The low polarization of the Mn-PBA@rGO/LTO-10% electrode at high current rates originates from the improved ionic and electronic conductive network compared to bare LTO electrode [38-40].

The first two galvanostatic discharge/charge curves of LTO and Mn-PBA@rGO/LTO–10% at 0.2 C are displayed in Fig. 4d. The first discharge and charge capacities of LTO electrode were high at 284.3 and 235.2 mAh g⁻¹, respectively, with an initial coulombic efficiency of 82.7%, due to the further intercalation of lithium ions into Li₇Ti₅O₁₂ to form Li₉Ti₅O₁₂ at low potential. Instead, for Mn-PBA@rGO/LTO–10%, the two voltage plateaus at 1.55 and 0.61 V indicated outstanding first discharge and charge capacities of 443.8 and 305.5 mAh g⁻¹, respectively. The more reversible specific capacity of PBA@rGO/LTO–10% composite occurred mainly in the voltage range from 0.5 to 1.5 V. The inferior initial coulombic efficiency of 68.8% resulted from parasitic reactions on the surface of Mn-PBA nanoparticles and can be seen in the difference in voltages of 1.6 and 2.4 V [41-43]. They originate from the formation of SEI films [44, 45] and the consumption of lithium ions at the electrochemically irreversible 48f sites in LTO [31]. Consequently, Mn-PBA@rGO/LTO–10% shows remarkable capacity loss during the first two cycles but no apparent capacity decrease at the voltage of 1.55 V, which corroborated the CV profiles in Fig. 3a.

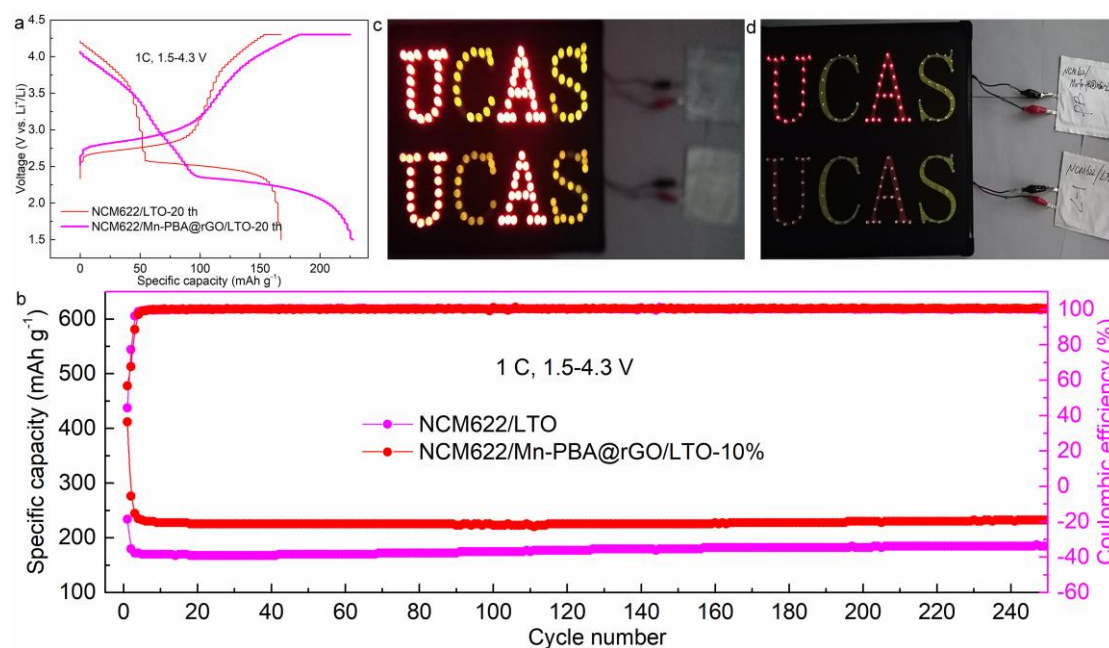


Figure 5. a) 20th charge/discharge curve and b) long-term cycling performance of NCM622/LTO and NCM622/Mn-PBA@rGO/LTO–10% full cells at 1 C in the 1.5–4.3 V voltage range. UCAS logo made of 37 red and 34 yellow light-emitting diodes (LEDs) in parallel powered by the NCM622/LTO (bottom) and NCM622/Mn-PBA@rGO/LTO–10% (top) full cells: c) Charging to 4.3 V after 150 cycles; d) Continuous discharge for 60 mins.

Fig. 4e shows the cycling performance of LTO and Mn-PBA@rGO/LTO–10% at a current rate of 0.5 C in the broad voltage range from 0.01 to 3 V. Notably, the specific capacity of Mn-PBA@rGO/LTO–10% rapidly increased from 288.5 to 360.4 mAh g⁻¹ after 150 cycles demonstrating a better cycling performance than pristine LTO electrode. This is due to the high theoretical capacity and enhanced lithium ion diffusion in Mn-PBA as well as the excellent electron transport ability in rGO. The coulombic efficiency of Mn-PBA@rGO/LTO–10% increased from 94.1% in the 2nd cycle to 99.3% in the 20th cycle, whereas it required 30 cycles for the pristine LTO electrode to reach 99.3%.

Subsequently, the coulombic efficiency of both samples stabilized at this value during the rest cycles, indicating good cycling stability of both the Mn-PBA@rGO/LTO-10% and the LTO electrodes. The long-term cycling performance of Mn-PBA@rGO/LTO-10% and LTO at high current rates of 5, 10, and 30 C for 400 cycles is shown in Fig. 4f. Mn-PBA@rGO/LTO-10% also had higher capacity retentions after 400 cycles of 112.3%, 104.5%, and 94.0% than pristine LTO (99.1%, 95.6%, and 71.7%) at 5, 10, and 30 C, respectively. This illustrates a better cyclability for Mn-PBA@rGO/LTO-10% than for LTO. Herein, the improved cycling performance of Mn-PBA@rGO/LTO-10% was attributed to the enhanced electron transport in rGO and lithium-ion diffusion in Mn-PBA that both from the composite. Compared to bare LTO, V-doped LTO and N-LTO@TiC/C composite material, the Mn-PBA@rGO/LTO composite anode material prepared herein possessed the best rate performance and cycling stability, as summarized in Table 1. The specific capacity of Mn-PBA@rGO/LTO was as high as 360 mAh g⁻¹ at 0.5 C after 150 cycles and 204 mAh g⁻¹ at 30 C after 400 cycles in the broad voltage range from 0.01 to 3 V because of the low polarization in the Mn-PBA@rGO/LTO composite. The use of a composite material could effectively increase the specific capacity of an LTO anode during excess discharge.

Table 1. Comparison of cycling and rate performance of LTO anode materials for LIBs.

Anode material	Rate (C)	Cycle number	Capacity (mAh g ⁻¹)	Ref.
LTO	1	300	160	[14]
	5	300	113	
Li ₄ Ti _{4.9} V _{0.1} O ₁₂	0.1	130	229	[15]
N-LTO@TiC/C	10	10000	143	[16]
	0.5	150	360	
Mn-PBA@rGO/LTO	5	400	278	This work
	10	400	247	
	30	400	204	

The outstanding electrochemical performance of Mn-PBA@rGO/LTO-10% composite anode was further tested in pouch cells using NCM622 as the cathode. The reversible specific capacity was calculated based on the mass of electroactive component in anode. Fig. 5a presents the 20th charge/discharge curve of NCM622/LTO and NCM622/Mn-PBA@rGO/LTO-10% full cells at 1 C in the 1.5–4.3 V voltage range. After 20 cycles, the NCM622/LTO and NCM622/Mn-PBA@rGO/LTO-10% full cells delivered discharge capacities of 167.5 and 227.7 mAh g⁻¹, respectively. The additional 60.2 mAh g⁻¹ was attributed to the Mn-PBA@rGO component and was mainly present for voltages between 2.3 and 3.5 V. Apparently, the specific capacity of NCM622/LTO and NCM622/Mn-PBA@rGO/LTO-10% decreased rapidly during the first three cycles, due to the irreversible consumption of lithium ions in NCM622. Subsequently, the two pouch cells showed excellent stability with a reversible specific capacity of 184.7 and 232.6 mAh g⁻¹ after 250 cycles, respectively, which corresponded to a coulombic efficiency of 100%. As shown in Figs. 5c and 5d, the UCAS logo consisting of 37 red LEDs (Power=1.8 V×20 mA×37=1.33 W) and 34 yellow LEDs

(Power=2 V×20 mA×34=1.36 W) in parallel could be efficiently powered by the assembled pouch cells. The LEDs powered by NCM622/Mn-PBA@rGO/LTO-10% were visibly brighter than those powered by NCM622/LTO cell once completely charged to 4.3 V (Fig. 5c). This was true even after a continuous discharge for 60 mins (Fig. 5d), suggesting a bright future for the application of the Mn-PBA@rGO/LTO-10% composite as batteries.

4. CONCLUSIONS

In conclusion, extending lithiation potential to near 0 V and fabricating composites with materials with good electronic and ionic conductive networks was very effective way to improve the specific capacity of LTO electrode. Mn-PBA@rGO has an high ionic conductivity and excellent electrical conductivity and could alleviate the large polarization in LTO at high current rates in a broad voltage window from 0.01 to 3 V. Ultimately, the Mn-PBA@rGO/LTO composite electrode showed a high specific capacity, very stable cyclability, and superior rate performance both in half cell and in a full battery. Therefore, Mn-PBA@rGO/LTO composite is a promising anode material for LIBs with the advantages of high specific capacity, and long cycling life.

ACKNOWLEDGEMENTS

Daming Sun and Huan Zhang contributed equally to this work. This work was supported by the National Natural Science Foundation of China (Grant No. 51474196, 21805053) and the CAS “Light of West China” Program. We would like to thank Mianzhong Chen and Chuanlan Peng for their kind guidance on preparing the pouch cells. Finally, we are very thankful to “ceshigo” (www.ceshigo.com) for their XPS and XRD characterization.

References

1. T. Ohzuku, A. Ueda, N. Yamamoto, *J. Electrochem. Soc.*, 142 (1995) 1431.
2. T. F. Yi, S. Y. Yang, Y. Xie, *J. Mater. Chem. A*, 3 (2015) 5750.
3. T. Yuan, Z. Tan, C. Ma, J. Yang, Z. F. Ma, S. Zheng, *Adv. Energy Mater.*, 7 (2017) 1601625.
4. H. Ge, N. Li, D. Li, C. Dai, D. Wang, *J. Phys. Chem. C*, 113 (2009) 6324.
5. E. Kang, Y. S. Jung, G. H. Kim, J. Chun, U. Wiesner, A.C. Dillon, J. K. Kim and J. Lee, *Adv. Funct. Mater.*, 21 (2011) 4349.
6. H. Gu, F. Chen, C. Liu, J. Qian, M. Ni, T. Liu, *J. Power Sources*, 369 (2017) 42.
7. B. N. Yun, H. L. Du, J. Y. Hwang, H. G. Jung, Y. K. Sun, *J. Mater. Chem. A*, 5 (2017) 2802.
8. K. Zhu, H. Gao, G. Hu, M. Liu, H. Wang, *J. Power Sources*, 340 (2017) 263.
9. C. Wang, S. Wang, L. Tang, Y. B. He, L. Gan, J. Li, H. D. Du, B. H. Li, Z. Q. Lin and F. Y. Kang, *Nano Energy*, 21 (2016) 133.
10. S. Repp, E. Harputlu, S. Gurgun, M. Castellano, N. Kremer, N. Pompe, J. worner, A. Hoffmann, R. Thoman, F. M. Emen, S. Weber, K. Ocakoglu and E. Erdem, *Nanoscale*, 10 (2018) 1877.
11. Q. Liang, N. Cao, Z. Song, X. Gao, L. Hou, T. Guo and X. Qin, *Electrochim. Acta*, 251 (2017) 407.
12. W. Li, T. L. Christiansen, C. Li, Y. Zhou, H. Fei, A. Mamakhel, B. B. Iversen and J. J. Watkins, *Nano Energy*, 52 (2018) 431.

13. M. R. Jo, J. Jung, G. H. Lee, Y. Kim, K. Song, J. Yang J. S. Chae, K. C. Roh, Y. Kim, W. S. Yoon and Y. M. Kang, *Nano Energy*, 19 (2016) 246.
14. C. Han, Y. B. He, S. Wang, C. Wang, H. Du, X. Qin, Z. Lin, B. Li and F. Kang, *Acs Appl. Mater. Interfaces*, 8 (2016) 18788.
15. T. F. Yi, J. Shu, Y. R. Zhu, X. D. Zhu, C. B. Yue, A. N. Zhou and R. S. Zhu, *Electrochimi. Acta*, 54 (2009) 7464.
16. Z. Yao, X. Xia, D. Xie, Y. Wang, C. A. Zhou, S. Liu, S. Deng, X. Wang and J. Tu, *Adv. Funct. Mater.*, 28 (2018) 1802756.
17. Y. Yang, S. Wang, M. Luo, W. Wang, F. Lv, Z. Tang and S. Guo, *J. Mater. Chem. A*, 5 (2017) 12096.
18. X. Lu, L. Zhao, X. He, R. Xiao, L. Gu, Y. S. Hu, H. Li, Z. Wang, X. Duan, L. Chen, J. Maier and Y. Ikuhara, *Adv. Mater.*, 24 (2012) 3233.
19. D. Ahn, X. Xiao, *Electrochem. Commun.*, 13 (2011) 796.
20. D. Sun, H. Wang, B. Deng, H. Zhang, L. Wang, Q. Wan, X. Yan and M. Qu, *Carbon*, 143 (2019) 706.
21. Y. Q. Wang, L. Guo, Y. G. Guo, H. Li, X. Q. He, S. Tsukimoto, Y. Ikuhara and L. Wan, *J. Am. Chem. Soc.*, 134 (2012) 7874.
22. M. Gockeln, S. Pokhrel, F. Meierhofer, J. Glenneberg, M. Schowalter, A. Rosenauer, U. Fritsching, M. Busse, L. Madler and R. Kun, *J. Power Sources*, 374 (2018) 97.
23. E. Zhao, C. Qin, H. R. Jung, G. Berdichevsky, A. Nese, S. Marder and G. Yushin, *ACS nano*, 10 (2016) 3977.
24. P. Nie, L. Shen, H. Luo, B. Ding, G. Xu, J. Wang and X. Zhang, *J. Mater. Chem. A*, 2 (2014) 5852.
25. Z. Qin, Y. Li, N. Gu, *Adv. Healthc. Mater.*, 7 (2018) 1800347.
26. A. J. Fernández-Ropero, M. J. Piernas-Muñoz, E. Castillo-Martínez, T. Rojo, M. Casas-Cabanas, *Electrochimi. Acta*, 210 (2016) 352.
27. D. Kong, W. Ren, Y. Luo, Y. Yang, C. Cheng, *J. Mater. Chem. A*, 2 (2014) 20221.
28. L. Shen, E. Uchaker, X. Zhang, G. Cao, *Adv. Mater.*, 24 (2012) 6502.
29. Z. Yao, X. Xia, Y. Zhong, Y. Wang, B. Zhang, D. Xie, X. Wang, J. Tu and Y. Huang, *J. Mater. Chem. A*, 5 (2017) 8916.
30. H. Xu, X. Hu, Y. Sun, W. Luo, C. Chen, Y. Liu and Y. Huang, *Nano Energy*, 10 (2014) 163.
31. R. Ma, L. Shao, K. Wu, M. Shui, D. Wang, J. Pan, N. Long, Y. Ren and J. Shu, *Acs Appl. Mater. Interfaces*, 5 (2013) 8615.
32. M. Huang, A. Xu, H. Duan, S. Wu, *J. Mater. Chem. A*, 6 (2018) 7155.
33. B. Sun, Z. Chen, H. S. Kim, H. Ahn, G. Wang, *J. Power Sources*, 196 (2011) 3346.
34. D. Pham Cong, J. S. Park, J. H. Kim, J. Kim, P. V. Braun, J. H. Choi, S. Choi, S. J. Kim, S. Y. Jeong and C. R. Cho, *Carbon*, 111 (2017) 28.
35. J. Zhang, Z. Xie, W. Li, S. Dong, M. Qu, *Carbon*, 74 (2014) 153.
36. L. Wang, Q. Xiao, L. Wu, G. Lei, Z. Li, *Solid State Ionics*, 236 (2013) 43.
37. H. Wang, D. Sun, X. Li, W. Ge, B. Deng, M. Qu and G. Peng, *Electrochimi. Acta*, 254 (2017) 112.
38. Y. Huang, M. Xie, J. Zhang, Z. Wang, Y. Jiang, G. Xiao, S. Li, L. Li, F. Wu and R. Chen, *Nano Energy*, 39 (2017) 273.
39. J. Kim, K. E. Lee, K. H. Kim, S. Wi, S. Lee, S. Nam, C. Kim, S. O. Kim and B. Park, *Carbon*, 114 (2017) 275-283.
40. C. Han, Y. B. He, M. Liu, B. Li, Q. H. Yang, C. P. Wong and F. Kang, *J. Mater. Chem. A*, 5 (2017) 6368.
41. L. Deng, Z. Yang, L. Tan, L. Zeng, Y. Zhu, L. Guo, *Adv. Mater.*, 30 (2018) 1802510.
42. F. C. Zhou, Y. H. Sun, J. Q. Li, J. M. Nan, *Appl. Surf. Sci.*, 444 (2018) 650.
43. M. Jose Piernas-Munoz, E. Castillo-Martinez, V. Roddatis, M. Armand, T. Rojo, *J. Power Sources*, 271 (2014) 489.
44. K. Qian, L. Tang, M. Wagemaker, Y. B. He, D. Liu, H. Li, R. Shi, B. Li and F. Kang, *Adv. Sci.*, 4

(2017) 1700205.

45. H. Ge, T. Hao, H. Osgood, B. Zhang, L. Chen, L. Cui, X. M. Song, O. Ogoke and G. Wu, *Acs Appl. Mater. Interfaces*, 8 (2016) 9162.

© 2019 The Authors. Published by ESG (www.electrochemsci.org). This article is an open access article distributed under the terms and conditions of the Creative Commons Attribution license (<http://creativecommons.org/licenses/by/4.0/>).